Quantitative analysis of twist boundaries and stacking faults in Bi-based superconductors by parallel recording of dark-field images with a coherent electron source

Lijun Wu,[1] Yimei Zhu,[1,*] J. Tafto,[1,2] D. O. Welch,[1] and M. Suenaga[1]
[1]*Materials Science Department, Brookhaven National Laboratory, Upton, New York 11973*
[2]*Department of Physics, University of Oslo, P.O. Box 1048 Blindern, N-0316 Oslo, Norway*
(Received 4 June 2002; published 19 September 2002)

Using a 300-keV transmission electron microscope equipped with a field-emission gun, we study grain boundaries by forming a coherent electron probe 100–200 μm above the specimen and observe in the diffraction mode the angular distribution of the transmitted electrons within the convergent beam disks. We studied Bi-based high-temperature superconductors containing stacking faults and twist grain boundaries with accompanying displacements perpendicular to the boundary plane. We observed strong intensity oscillation from the planar faults even when they were viewed edge on, in agreement with model calculations. At twist boundaries we observed rigid body translation normal to the boundaries as large as 0.03 ± 0.01 nm, and determined the displacement vector associated with the addition or subtraction of one bilayer of $(CuO_2 + Ca)$ to be 0.320 ± 0.002 nm for the intrinsic and extrinsic layers in $Bi_2Sr_2CaCu_2O_8$, as well as for the intrinsic layer in $Bi_2Sr_2Ca_2Cu_3O_{10}$. We also briefly address the possibility of determining the profile of the inner potential across grain boundaries using this coherent electron probe.

DOI: 10.1103/PhysRevB.66.104517 PACS number(s): 61.72.Nn, 61.14.Lj, 74.72.Hs

I. INTRODUCTION

The presence of defects strongly influences the properties of the high-temperature superconductors,[1] in particular their current carrying capacities.[2,3] Thus a major challenge we face is to identify the factors that limit the current density. It is known that stacking faults and grain boundaries play an important role in determining the superconducting transport properties, and substantial efforts have been made into recognizing the effects of different types of two-dimensional defects.[4–7] Two variables that characterize a grain boundary are its inner potential and lattice displacement such as rigid body translation that are a consequence of the modified local atomic arrangement at the boundary. Thus accurate measurements of the displacement vector and inner potential distribution are of great importance in understanding grain boundaries. Knowledge of this rigid body translation is a particularly useful constraint in theoretical studies and atomistic computer simulations of the grain-boundary structure.[8]

For the high-temperature superconductors there has been only modest success in growing large perfect single crystals, not to mention ideal bicrystals of bulk materials with sufficient high quality to perform quantitative experiments using synchrotron x rays. Thus the major technique to address the structure of grain boundaries and planar faults in these materials has been transmission electron microscopy (TEM), both in diffraction and imaging. Up to now, measurements of interfacial displacement on the atomic scale have been focused on the use of high-resolution electron microscopy (HREM), however, due to the presence of third- and higher-order astigmatism of the objective lens the accuracy of the measurements obtained is often insufficient. Outside the electron microscope community, at least, these techniques are considered rather qualitative. In the present study we use an alternative TEM technique. Our transmission electron microscope is equipped with a coherent electron source that we take advantage of to perform *coherent* convergent beam electron diffraction.[9,10] With this technique, which was briefly described recently,[11] we determine displacement vectors at grain boundaries and planar faults with accuracy that is an order of magnitude higher than using any established electron microscopy techniques.

We study grain boundaries and planar faults in the Bi-based high-temperature superconductors. The Bi-based superconductors form a homologous series $Bi_2Sr_2Ca_{m-1}Cu_mO_{4+2m+\delta}$ ($m=1$, 2, or 3).[12,13] The superconducting transition temperatures of these cuprates are: $T_c \approx 10$ K for $m=1$, i.e., $Bi_2Sr_2CuO_6$ (hereafter denoted Bi2201), $T_c \approx 80$ K for $m=2$, i.e., $Bi_2Sr_2CaCu_2O_8$ (Bi2212), and $T_c \approx 110$ K for $m=3$, i.e., $Bi_2Sr_2Ca_2Cu_3O_{10}$ (Bi2223). These phases have structural similarities with lattice parameters $a \approx b = 0.54$ nm. The stacking along the c axis differs for the three phases, and can be considered as consisting of sequences of about 0.22-nm-thick oxide layers: BiO-BiO-SrO-CuO_2-$(m-1)$[Ca-CuO_2]-SrO-BiO-BiO ($m=1,2,3$). The repetition of this sequence is half a unit cell along the c axis owing to a glide plane in the crystal unit cell. The number of layers in one unit cell is 10 ($m=1$), 14 ($m=2$), and 18 ($m=3$), respectively, and their lattice parameters are: $a^{Bi2201}=0.5361$ nm, $b^{Bi2201}=0.5370$ nm, $c^{Bi2201}=2.4369$ nm,[14] $a^{Bi2212}=0.5408$ nm, $b^{Bi2212}=0.5413$ nm, $c^{Bi2212}=3.0871$ nm,[15] and $a^{Bi2223}=0.540\,29$ nm, $b^{Bi2223}=0.541\,54$ nm, and $c^{Bi2223}=3.7074$ nm.[16]

Addition or subtraction of a slab, consisting of a CuO_2– and a Ca layer, hereafter referred to as a $(CuO_2 + Ca)$ bilayer, is the most common defect in Bi-based superconductors. We mostly studied Bi2212. Here subtraction and addition of a slab of $(CuO_2 + Ca)$ can be looked upon as resulting in an intercalated layer of thickness half the lattice parameter along the c axis of the Bi2201 and Bi2223 phases, respectively. Along the long c axis, i.e., (001) direction in these pseudotetragonal crystal structures, the bonding between the

adjacent BiO planes are rather weak. Thus between these two planes the crystal is prone to the formation of twist grain boundaries in polycrystalline Bi2212. Also present are asymmetrical tilt boundaries and boundaries with both tilt and twist components with one of the adjoining crystal grains tending to terminate on the *a*-*b* plane, while symmetrical tilt boundaries are rare.

This paper is organized as follows: After a brief orientation about the specimen fabrication procedure and the transmission electron microscope experiments, we describe in some detail the technique of coherent convergent beam electron diffraction that is used to extract comprehensive information about defects in materials. We then present experimental results and interpret these for planar faults and twist grain boundaries in Bi-based superconductors, followed by a discussion. A short derivation of the lattice displacement at a twist boundary related to the interfacial energy of the boundary and surface energy of the crystal is included in the Appendix.

II. EXPERIMENT

The material we studied was *c*-axis aligned Bi-cuprate platelets from Ag-sheathed tape, fabricated through the powder-in-tube process.[17] TEM samples were prepared using a dedicated mechanical polishing technique that provides large area of view, and subsequently ion milled. Coherent convergent beam electron diffraction (CBED) patterns were obtained at 300 keV with our JEOL 3000F transmission electron microscope equipped with a field-emission gun and a Gatan imaging filter (GIF). Most of the coherent CBED patterns were recorded using a Fuji FDL5000 imaging-plate system, which gives an area of view equal to a conventional photographic film, while selected CBED disks were energy filtered and recorded using a charge-coupled device (CCD) camera. The experimental procedure we use differs from conventional CBED in two ways: We focus the incident electrons to form a crossover above the specimen with a convergent beam angle small enough to avoid overlap between the diffraction disks associated with the individual reflections. This ensures that each of the nonoverlapping diffraction disks form a shadow image of the specimen with reciprocal- as well as real-space information (Fig. 1). The other way the procedure differs from the traditional approach of obtaining a CBED pattern is that the probe is coherent, which turns out to be particularly useful to address the rigid body translation at planar faults and grain boundaries when these are viewed edge on. We have previously focused an *incoherent* probe above the edge of a wedge-shaped, defect-free specimen to study the intensity oscillations as a function of thickness in different reflections. The purpose of those experiments was to study charge transfer in high-temperature superconductors by accurately determining the structure factors of low-order reflections.[18–20]

III. COHERENT CBED: CONTRAST UNDER COHERENT ILLUMINATION

Convergent beam electron diffraction (CBED) patterns that are recorded with coherent and incoherent illumination may differ greatly when defects are present within the illuminated area of the crystal. On the other hand, CBED patterns from a perfect crystal are virtually the same with a coherent and an incoherent electron source when the CBED disks do not overlap. This may be explained by realizing that a certain point within a CBED disk receives contributions from only one direction within the incident-beam cone when the crystal is perfect because then there is no diffuse scattering due to defects. However, when defects and deviation from perfect periodicity are present within the illuminated area of the specimen, there are no longer only delta-function-like reciprocal vectors. Thus different incident beam directions within the CBED cone contribute to the amplitude at a particular point in the CBED disk. Hence, even when the disks do not overlap, coherent and incoherent probes give different results for crystals with faults.[9] We now briefly present the way we calculate coherent beam electron-diffraction patterns and illustrate this by showing examples of calculations for a simple model.

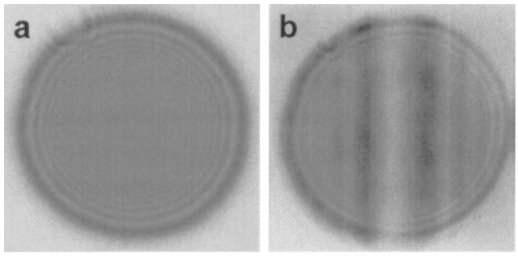

FIG. 1. Examples of shadow images of the coherent convergent beam electron diffraction recorded in the back focal plane of the objective lens in a microscope with a field-emission gun. (a) (000) disk in vacuum, i.e., without specimen; (b) (008) reflection from an area consisting a stacking fault in Bi2212. Note that the intensity oscillation at the rim of the disks is due to the wave interference from the condenser aperture, while the vertical fringes are due to the existence of the fault.

A. Calculations

A comprehensive dynamical calculation, including anomalous absorption, of the coherent CBED pattern for a sample containing defects is a formidable task, so we limit this study to kinematical diffraction. Experimentally we found that our measurements of displacement vectors were insensitive to small variations in sample thickness and crystallographic direction of the incident beam (varying set of excitation errors for the reflections). Thus this approach is reliable and robust with respect to extracting values for the parameter we are going to measure, namely the rigid body translation vector **R**.

1. Contrast from lattice displacement

We explain the calculation procedure for the kinematical coherent convergent beam electron-diffraction pattern from a sample containing a planar fault by referring to a schematic in Fig. 2. The short vertical planes represent the *a*-*b* planes with periodicity *c* in the thin crystal normal to the incident beam direction. *H* is the distance from the source or cross-

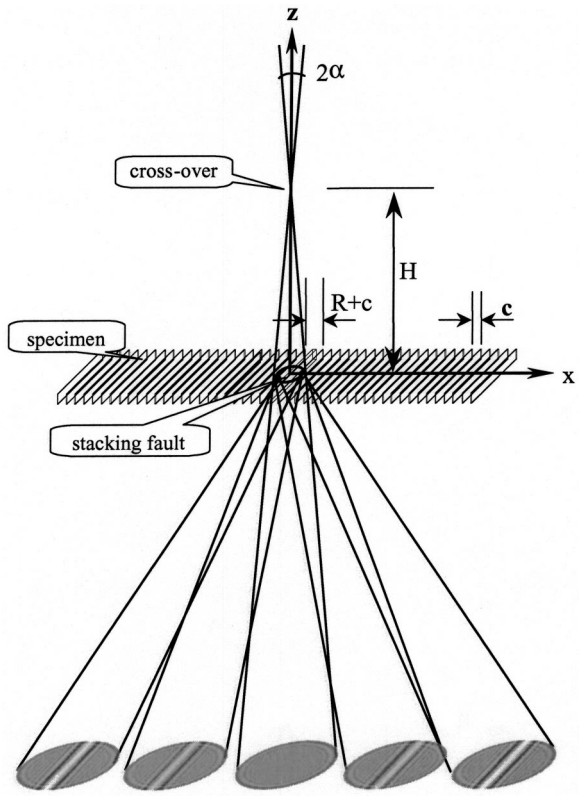

FIG. 2. Schematic of the experimental setup showing how the phase of the electrons that are scattered into a particular direction 2α changes for different paths from the crossover through the specimen. The vertical planes represent atom planes separated by a spacing c. H is the distance from the source or crossover to the specimen, R the horizontal displacement at the fault that is placed at the vertical mirror in the figure, and 2α the angle relative to the vertical axis.

over to the specimen, R the horizontal displacement at the fault, and 2α is the angle relative to the vertical axis. We calculate the amplitude and intensity at infinite distance, which is equivalent to the diffraction pattern in the back focal plane of the objective lens, by considering the phase difference for different paths through the specimen. Below the specimen the amplitude at infinite distance in the kinematical or single-scattering approximation for a three-dimensional case becomes

$$\psi_g = \sum_{m,n,p} F_g \exp 2\pi i \left(\frac{|\mathbf{r}+\mathbf{H}|}{\lambda_0} - \mathbf{r}\cdot\mathbf{g} \right). \tag{1}$$

Here λ_0 is the wavelength of incident electrons, F_g is the structure factor, reciprocal vector $\mathbf{g}=h\mathbf{a}^*+k\mathbf{b}^*+l\mathbf{c}^*$, and the position vector of lattice,

$$\mathbf{r}=\begin{cases} p\mathbf{a}+m\mathbf{b}+(n-N)\mathbf{c}-(\mathbf{c}/2+\mathbf{R}/2) & n\leqslant N \\ p\mathbf{a}+m\mathbf{b}+(n-N-1)\mathbf{c}+(\mathbf{c}/2+\mathbf{R}/2) & n>N \end{cases}, \tag{2}$$

where m,n,p are integers and $\mathbf{a}$, $\mathbf{b}$, $\mathbf{c}$ are orthogonal direction vectors of the system. The summation is over the whole illuminated area of the specimen, that is, $|\mathbf{r}|\leqslant r_{\max}$ where $r_{\max}$ is the radius of the beam at the specimen with $N=(2r_{\max}+c-R)/2c$. The convergent beam angle is $2\alpha\approx 2r_{\max}/H$.

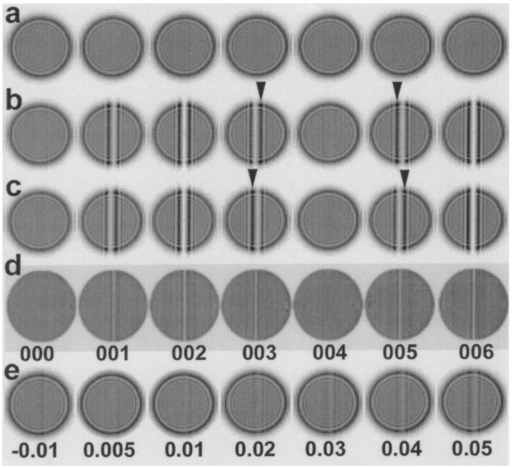

FIG. 3. The effect of the displacement R and the distance H between the crossover and the specimen. (a) $R=0$, $H=160$ μm. (b) $R=c/4$, $H=160$ μm. (c) $R=-c/4$, $H=160$ μm, and (d) $R=c/4$, $H=1600$ μm. The arrow pairs in (b) and (c) indicate the asymmetry of the fault contrast, which can be used to determine the sign of the displacement. (e) The effect of Δn on the fault contrast. Note that the fault contrast is clearly visible for $\Delta n \geqslant 0.02$.

Figure 3 shows the calculated shadow images of a systematic row of reflections (0th–6th order), using a model crystal containing a set of identical lattice planes with a planar defect in the middle, similar to that in Fig. 2. It demonstrates the effect on the diffraction pattern of the displacement vector $\mathbf{R}$ and height from specimen to crossover H. For $R=0$, the calculated shadow images, Fig. 3(a), only show rings of interference fringes similar to Fresnel diffraction from a circular aperture. For a lattice displacement along the plane normal with an amplitude $R=+c/4$, we see Fresnel fringes parallel to the defect in the reflection $\mathbf{g}$ of 001, 002, 003, and 005, but not in 004 where $\mathbf{g}\cdot\mathbf{R}$ is an integer, Fig. 3(b). The strongest contrast occurs at the 002 reflection where $\mathbf{g}\cdot\mathbf{R}=0.5$. We also note that the fringes are asymmetric for all odd reflections, a feature that can be used to determine the sign of the displacement. The thick black fringe, indicated by arrow heads in Fig. 3(b), is on the right-hand side of the defect for the 003 reflection and on the left-hand side for the 005 reflection when the displacement is positive, or tensile. The asymmetry is reversed for a negative displacement, or compression, $R=-c/4$, Fig. 3(c). Also, by comparing the calculated patterns in Figs. 3(b) and (c) with Fig. 3(d) we note that increasing the distance H from the crossover to the specimen makes little difference in the overall shadow images, but the intensity oscillations are confined to a smaller angle for large H. This is related to the magnification within the shadow images or diffraction disks. For very large H, when each disc corresponds to a conventional dark-field image, the contrast from the fault is confined to a very small angle, and thus difficult to see when the fault is observed edge on. Note the similarities with conventional dark-field imaging using a particular reflection where there is no contrast from displacement when $\mathbf{g}\cdot\mathbf{R}$ is an integer.

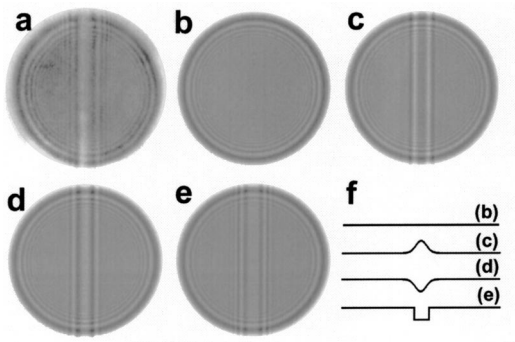

FIG. 4. Experiment and calculations of the inner potential across a grain boundary in Bi2212. (a) experimental (000) disk. (b)–(e) calculations with various interfacial potentials shown in (f). The maximum amplitude of the potential is 2 V and the full width at half maximum is 1 nm. The sample thickness is 40 nm.

The calculations we presented in Fig. 3 are with a perfectly coherent point source. In our experiments the probe formed at crossover is not completely coherent. Thus we convolute the calculated patterns with a Gaussian beam-spread function before comparing the results of the calculations with our experimental observations.

2. Contrast from mean inner potential variations across planar boundaries

An important, though not a central topic in this study, is the inner potential across grain boundaries and across interfaces between dissimilar phases. Figure 4(a) shows the energy filtered 000 disc from an area with a twist boundary in $Bi_2Sr_2CaCu_2O_8$. The twist is around the *c* axis, and also in this case the incident-beam direction is normal to the *c* axis. The reason why we focus attention on the 000 disc is that the mean inner potential mainly influences the scattering at small scattering angle, i.e., close to the forward direction. When we look at the 000 disk we need not consider the crystallinity of the material in the thin crystal limit where the kinematical theory applies, and the intensity distribution of the 000 disc is not affected by displacement. On propagating through the thin foil the electrons undergo a phase shift $2\pi z/\lambda_m$ where λ_m is the wavelength of the electron in the material and *z* is the thickness. The electron wavelength in a material is given by

$$\lambda_m = \lambda_0 \left(1 - \frac{U}{E}\right)^{-1/2}. \tag{3}$$

Here λ_0 is the electron wavelength in vacuum, *U* is the attractive (negative) mean inner potential seen by the electron, and *E* is the accelerating voltage of the microscope. Let the inner potential and thus λ_m be uniform through the thickness of the specimen, but the inner potential as well as the thickness *z* be a function of the transversal position (*x*,*y*) on the specimen. We thus get an additional term in the exponent in Eq. (1). Because we now do not deal with discrete atomic planes, we formally need to write this as an integral, although in computation we divide the illuminated area into finite elements:

$$\psi(\mathbf{s}) = \int\int_{\text{specimen}} \exp\left[2\pi i\left(\frac{\sqrt{x^2+y^2+H^2}}{\lambda_0} - xs_x - ys_y + \frac{z(x,y)}{\lambda_m(x,y)} + \frac{z_{\max} - z(x,y)}{\lambda_0}\right)\right] dxdy. \tag{4}$$

$\mathbf{s} = s_x\mathbf{i} + s_y\mathbf{j}$ is the coordinate within the 000 disk, and $z_{\max}$ the maximum thickness of the specimen. We may choose any constant for $z_{\max}$; we need only to ensure that the electrons that have propagated a shorter distance Δz through the specimen have propagated the corresponding larger distance Δz through vacuum.

In the calculation in Fig. 4(b) there is no inner potential or thickness variation across the illuminated area of the specimen. In Fig. 4(c) the electrons see a deeper potential well of depth 2 eV and width 1 nm (full width at half maximum) at the boundary [Fig. 4(f)]. In Fig. 4(d) we have only reversed the sign of the potential change at the boundary. In Fig. 4(e) we have interchanged the Gaussian profile, which describes the inner potential variation in Fig. 4(d), with a hat function. Figure 4(e) appears to agree fairly well with the observation of Fig. 4(a). Here the potential at the interface is closer to that of vacuum than is the case in the matrix. The reason for this may be a more open structure at the interface or electron transfer to the interface area. Quantitative analysis of the inner potential variation across interfaces is challenging in the sense that the measured projected potential is sensitive to the local thickness and other parameters. Nevertheless, the measurements are in good agreement with an independent study of space charge in Bi2212 twist boundaries using off-axis electron holography that gives an average value of the boundaries potential of 2.18 V and the boundary width of 0.86 nm.[21] However, the advantage of the technique used in here is that we observe many dark-field shadow images simultaneously. Since lattice displacement contributes only to the intensity in the reflections, not the direct, or zero-order, beam, by examining the intensity oscillation of the boundary in the zero-order beam we can determine the interfacial potential without the knowledge of lattice distortion across the boundary.

B. Error analysis

In this work, where we study displacements along the *c* axis of Bi2212 with the large dimension of the unit cell, we are in the fortunate situation that this reciprocal row is very densely populated with reflections. Thus we can simultaneously probe the contrast of many reflections. The planar fault that we barely see in the real-space image of a Bi2212 sample in Fig. 5(a) is clearly visible in Fig. 5(b) that shows a coherent CBED pattern where fringes from the planar fault show up simultaneously in more than 60 reflections in a single acquisition. Similar to the extinction criterion that is used for bright- and dark-field imaging in conventional TEM, the fault in the shadow images is out of contrast when the scalar product $\mathbf{g}\cdot\mathbf{R}$ is equal, or close to, an integer *n*. This is nearly the case for the (0,0,10), (0,0,20), (0,0,28), and (0,0,30) reflection in Fig. 5(b) in the $[-110]$ projection of

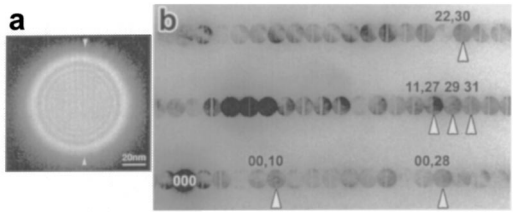

FIG. 5. An extrinsic stacking due to the intercalation of a (CuO_2+Ca) layer in Bi2212. (a) A real-space image (002 lattice fringes) with the crossover above the sample, showing a wide lattice fringe at the location of the fault denoted by arrows. (b) Diffraction pattern near the $(-110)^*$ zone, recorded with an imaging plate system, showing high-order reflections. Note that reflections with $l=10$, 28, and 30 show weak contrast, but the most featureless reflection is $l=29$.

Bi2212. The sensitivity gets higher farther out in reciprocal space and that is why we see noticeable contrast in (0,0,30), but not in (0,0,10), while in (1,1,29) there is no visible contrast. The displacement vector is thus $R=(30/29)(c/10)=0.320$ nm. A very conservative estimate of the accuracy is 0.320 nm/29=0.01 nm based on the fact that we clearly see contrast in the (0,0,28) and (0,0,30) reflection in Fig. 5(b). In general terms the error in such a measurement can be assessed from visual inspection, i.e., whether the fault is out of contrast in a particular g of mth, or $(m\pm1)$th, order. Then, the error in the displacement vector is R/m. Evidently, the accuracy improves with the order of the reflection. In the case that there is a weak, residual contrast of the fault, e.g., where the complete extinction of fault contrast is associated with a forbidden reflection, or a reflection not present in the diffraction pattern, the criterion $|g\cdot R-n|<\Delta n$ can be used to estimate error in measurement. The error ΔR can then be expressed by

$$|\Delta R|=|\Delta n/g|, \tag{5}$$

where Δn is the deviation from the integer n, and g is the nth-order reflection in which the minimum contrast exists. Figure 3(e) shows the residual contrast for $\Delta n=-0.01-0.05$ for an arbitrary reflection which can be used as a guideline to estimate the measurement error. We note that for $\Delta n\geqslant 0.02$, the fault exhibits visible contrast. The same value applies to conventional bright-field imaging in TEM.[8] Thus, in practice, without the simulation, we can estimate the measurement error associated with Δn for the shadow images with or without complete extinction of the fault contrast. The extinction criterion works best for displacement vectors R larger than $c/40$ which corresponds to 0.08 nm because it is hard to observe the contrast and thus extinction of contrast farther out in reciprocal space than the (0,0,40) reflection in these cuprates. With the inherent redundancy in the experimental data set caused by the fact that we observe many diffraction disks simultaneously, we can achieve much higher accuracy in the measured values of displacement vectors. Quantitative error analysis procedures were undertaken by first calculating the shadow images of a large number of reflections, then comparing these results with observations. For a planar fault, a line scan of many experimental shadow

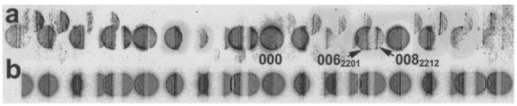

FIG. 6. Coherent CBED when the electrons from the crossover illuminate a (001) interface region between Bi2201 and Bi2212. (a) Experiment; (b) calculation. Note that the weak disk contrast above the $(00l)$ systematic row in (a) is due to the superlattice reflection of the structural modulation in Bi2212.

images can be compared with the calculated ones with different values to search for the best fit to determine the displacement **R**. Finally, the comparison, or the goodness of fit, was refined using a least-square-fitting procedure by finding the minimum in a best-fit parameter χ^2 as a function of adjustable parameters, where $\chi^2=\Sigma(I^{\rm exp}-I^{\rm cal})^2/\Sigma(I^{\rm exp})^2$.

IV. OBSERVATIONS AND INTERPRETATION OF INTERFACES AND PLANAR DEFECTS

A. Interface between Bi2201 and Bi2212

In Bi2212, sometimes we observe local Bi2201 phase which lacks two (CuO_2+Ca) layers for each unit cell, resulting in c^{2201} being 0.65 nm shorter than c^{2212}. In experiment, we have placed the coherent probe above a planar interface between Bi2201 and Bi2212 with the interface normal along the c axis, we observe an interesting pattern with two half-disks, each represents one side of the boundary, varying their overlapping regions with reflections [Fig. 6(a)]. The incident beam is here, as in the following experiments we will present, normal to the c axis so that the fault is viewed edge on. Note that the weak disk contrast shown above the systematic row of the $(00l)$ Bragg reflections in the pattern results form the superlattice reflections due to the structural modulation of the crystal. In Fig. 6(b) we compare with calculations based on assuming a planar spacing of $c^{2212}/2$ on the right-hand side of the illuminated disk on the specimen, and $c^{2201}/2$ on the left-hand side. The agreement with the experiment is quite good by including only these two lattice parameters in addition to the height H from specimen to crossover, which is the only adjustable parameter. The good fit suggests that this simple kinematical approach is sufficient to calculate the fringe contrast from planar faults caused by the coherence of the electron probe.

B. Intercalated layers/stacking faults

To the first approximation we may expect the displacement for the intrinsic fault in Bi2212 which corresponds to a layer of thickness half a unit of Bi2212 being replaced by half a unit cell of Bi2201 resulting in $R_1=1/2(c^{2201}-c^{2212})=-0.325$ nm. Similarly for the extrinsic fault in Bi2212 $R_2=1/2(c^{2223}-c^{2212})=0.310$ nm, and the intrinsic fault in Bi2223 $R_3=1/2(c^{2212}-c^{2223})=-0.310$ nm. We now present the experiments and determine these displacement vectors based on comparison with calculations.

1. The intrinsic stacking fault in Bi2212

Figure 7(a) shows a coherent diffraction from an area with a planar defect near the $(-110)^*$ zone. Examination of the

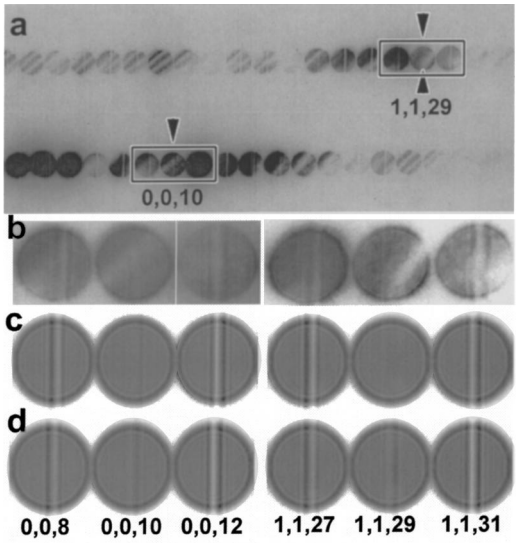

FIG. 7. An intrinsic stacking fault due to the lack of a (CuO_2 + Ca) layer in Bi2212. (a) Diffraction pattern near the $(-110)^*$ zone recorded. (b) Enlarged reflections of 008, 0010, 0012, and 1127, 1129, and 1131 from (a). Note that the 0012 in (a) was replaced by the one in (b) with shorter exposure. (c) and (d) Calculated reflections for $R=-0.3195$ nm (c) and $R=-0.325$ nm (d).

pattern shows that the fault contrast is very weak in the 0,0,10 reflection and because all the reflections with smaller l exhibited clear contrast, the displacement vector is around 3.089 nm/10=0.309 nm. The contrast asymmetry is such that the intensity of the fringes in 0,0,8 and 0,0,12 reflection is strong on the sides facing away from the 0010 reflection, suggesting an intrinsic fault. This asymmetry in the contrast as well as the value of the displacement vector are consistent with the lack of the (CuO_2+Ca) bilayer in Bi2212, or the intercalation of a half unit cell of Bi2201 in a Bi2212 matrix. Further out in reciprocal space the sensitivity to displacement is higher, and for this fault there was no visible contrast in the 1,1,29 reflection, as shown in Fig. 7(b). Simulation using the displacement that equals to difference of the c lattice parameters between Bi2201 and Bi2212 $R_1=1/2(c^{2201}-c^{2212})=-0.325$ nm does not give good fit to the experiment since the fault contrast in the 1129 reflection is too strong. By comparison between experiment and calculations with the refinement procedure we described above, we arrived at the conclusion that $R=-0.3195\pm0.0010$ nm, as indicated in Fig. 7(c).

2. The extrinsic stacking fault in Bi2212

Figure 8(a) shows another example of a planar fault recorded with an imaging plate system. For comparison, a CCD camera was also used to record selected disks. In Fig. 8(a) the asymmetry of the fringe contrast from the fault is reversed compared with the coherent diffraction pattern in Fig. 7(a). The reversed positions of the vertical, thick black fringes in the 008 and 0010 reflections are the most evident, suggesting a positive displacement. It is this type of fault that was shown in Fig. 5(a). By comparing with calculations, Figs. 8(b)–(e), we arrive at a displacement vector $R=0.320$

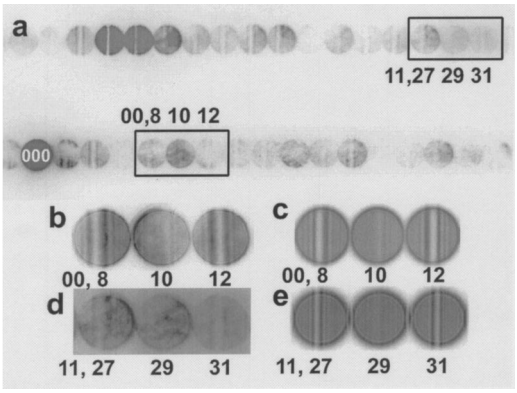

FIG. 8. An extrinsic stacking fault in Bi2212. (a) Experimental diffraction pattern of the $(-110)^*$ zone recorded with an imaging plate system. The same reflections in the box areas in (a) recorded in a CCD camera are shown in (b) and (d). Calculated patterns using the kinematical approach with $R=0.320$ nm are shown in (c) and (e).

±0.002 nm. We encountered many of this type of fault in our specimens, and all exhibited the same contrast regardless, of the difference in thickness and in crystallographic orientation with respect to the incident-beam direction. The only requirement appeared to be that the reflections along the c axis are visible, and preferably other reciprocal rows parallel to c^* to observe high-order reflections with $l=2n+1$.

3. The intrinsic stacking fault in Bi2223

We also measured the displacement of the intrinsic fault in Bi2223 where a single (CuO_2+Ca) bilayer was absent, forming locally a slab of structure of Bi2212, i.e., an intercalation of half unit cell of Bi2212 in the Bi2223 matrix. Figure 9 are the experimental shadow images covering an area with such a fault near the [−110] projection. Very weak intensities of the fault were observed for the 0012, 0024, and 1123 reflections. Among them, 1,1,23 has the least contrast, which gives the displacement $R=(2/23)d^{2223}=0.322$ nm. The sign of the displacement was determined by the simulation shown in Figs. 9(b) and (c), with $R=-0.322$ nm for contraction and $R=+0.322$ nm for expansion, respectively. The calculated asymmetry of the fault fringes for the dis-

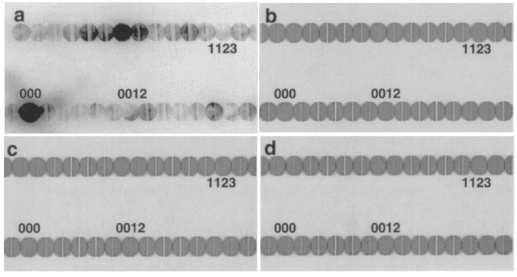

FIG. 9. An intrinsic stacking fault due to the lack of a (CuO_2 + Ca) layer in Bi2223. (a) Diffraction pattern near the $(-110)^*$ zone recorded with an imaging plate system. (b)–(d) Calculated reflections for $R=-0.322$ nm (b), which gives the best match with the experimental observations, $R=0.322$ nm (c), and $R=-0.310$ nm (d).

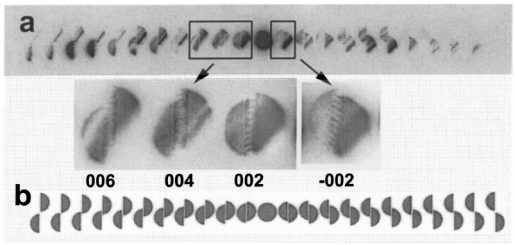

FIG. 10. A small-angle tilt boundary in Bi2212. (a) Experiment; (b) calculation. Note the fine periodic fringes running out of the boundary that are caused by the grain-boundary dislocations.

placement with a negative sign [Fig. 9(b)] shows good agreement with the experimental observation in Fig. 9(a). On the other hand, the simulated pattern using the difference in the *c*-lattice parameter between Bi2212 and Bi2223, i.e. $R=-(c^{2223}-c^{2212})/2=-0.310$ nm, Fig. 9(d), does not match with the experimental observation because the fault contrast in 1123 is too strong, while that in 0024 is too weak. Using the residual-contrast criterion, we estimated a measurement error to $\Delta R=\pm 0.003$ nm.

C. Grain boundaries

We now move on to grain boundaries, focusing on (001) twist boundaries. At grain boundaries an expansion may be expected.[17] In the Bi2212 superconductors we frequently encounter a single stacking fault, either extrinsic or intrinsic at twist grain boundaries, as shown in Figs. 4 and 5 in Ref. 7. It is worth noting that our technique measures the overall, or integrated, displacement across the boundary, thus the displacement value we obtain will then be the sum of that from the stacking fault as well as from the grain boundary. Fortunately, since now that we have measured the displacement vector associated with intrinsic and extrinsic stacking faults, the displacement due to the boundary can be determined.

1. Tilt boundaries

Figure 10 shows a coherent CBED from a small-angle tilt grain boundary in Bi2212, formed by a rotation of 5° about the *b* axis. The misorientation angle can be easily measured from the splitting angle of the reflections representing each side of the crystal across the boundary. There is interesting periodic-fringe contrast running out from the boundary, or the split interface of the half disks. The periodicity of the fringe contrast decreases with the increase of the order of the reflections. We attribute the contrast to the strain field, or a dislocation array, at the boundary. Using the Frank formula, $d=|\mathbf{b}|/\sin\theta$ (where d and $\mathbf{b}$ are the spacing and the Burgers vector of the grain-boundary dislocations, and θ is the misorientation across the boundary. Using a simple geometric model, we calculated the shadow image of the coherent diffraction pattern [Fig. 10(b)], which is in good agreement with the experiment [Fig. 10(a)], further suggesting the capabilities of the technique in studying interfaces and grain boundaries.

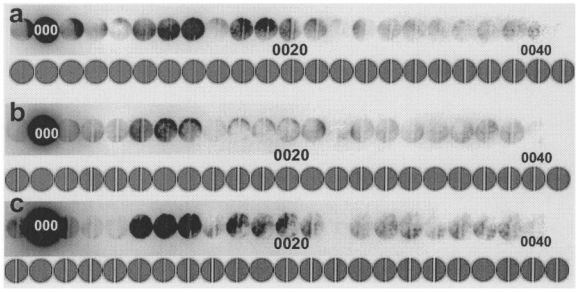

FIG. 11. Experimental shadow images of (001) twist boundaries in Bi2212 in coherent convergent beam electron diffraction for various misorientation angle θ. The corresponding calculation is listed below. (a) $\theta=23.7°$ with $R_e=0.026$ nm, (b) $\theta=17.2°$ with $R_{\text{total}}=-0.285$ nm. (c) $\theta=11.5°$ with $R_{\text{total}}=0.345$ nm.

2. Twist boundaries in Bi2212

We now present our experimental results on the rigid body translation at twist boundaries. The three examples we show here are all pure (001) twist boundaries with misorientation angles ranging from 11–24°, as defined by the crystallographic orientation of the grains relative to each other. We start with an example with no intercalation at the boundary, Fig. 11(a), with calculation shown below the experimental observations. We then show a boundary with an additional intrinsic stacking fault at the boundary, Fig. 11(b), and finally a twist boundary with an extrinsic stacking fault, Fig. 11(c).

Figure 11(a) is coherent diffraction pattern from a twist boundary with a geometry close to $\Sigma 13$. The two grains across the boundary were rotated 23.7° about the *c* axis with the (001) plane as its interfacial plane. We note in Fig. 11(a) that the contrast in the 002 disk is hardly visible, but increases gradually out to at least 0,0,30 in experiment. This trend is clearly demonstrated in the calculation. At even larger reciprocal distances, or in high-order reflections, we see the contrast from the fault, but local distortions and poor signal/noise ratio make it hard to assess the amplitude of the contrast. For reflections closer to the 000 disk than 0,0,30 reflection, the asymmetry of the contrast is consistently visible with the dark side of the fringes facing the 000 disk, showing with reference to Fig. 3 that there is an expansion at the boundary. We did calculations with different values of the displacement vector $\mathbf{R}$ and arrived at an expansion $\mathbf{R}_e=0.026\pm 0.004$ nm.

Figure 11(b) shows another example of a 17.2° twist boundary with geometry close to $\Sigma 25$, however, the boundary has a stacking fault adjacent to it, as clearly seen in the real-space image. In the experimental pattern we see from the asymmetry of the contrast that the fault is intrinsic with nearly extinction of contrast at 0,0,10 and 0,0,22 which corresponds of to $R_{\text{total}}=-0.2810$ nm. This value deviates from $R=-0.3195$ nm we observed for an intrinsic stacking fault. We attribute the additional 0.038 nm to expansion at the twist boundary. In the calculation, we find the best fit to be $R_{\text{total}}=-0.285$ nm and thus an expansion from the twisting is $\mathbf{R}_e=0.03$ nm.

A (001) twist grain boundary (11.5°, $\sim\Sigma 41$) also associated with a stacking fault is shown in Fig. 11(c). The asymmetry and extinction in Fig. 11(c) suggest a positive rigid body translation. Through comparison with calculations we found the resultant displacement vector is $R_{\text{total}} = +0.345$ nm, suggesting an extrinsic stacking fault with $R = 0.320$ nm and in addition an expansion of $\mathbf{R}_e = 0.025$ nm.

V. DISCUSSION

In this study by coherent beam electron diffraction of Bi2212, we find the displacement vectors $R = -0.3195 \pm 0.0010$ nm and $R = 0.320 \pm 0.002$ nm resulting from subtraction and addition of a slab of $(CuO_2 + Ca)$ bilayer, i.e., an intrinsic and extrinsic stacking fault, respectively. Likewise the subtraction of such a bilayer from Bi2223 results in the rigid body translation of $R = -0.322 \pm 0.003$ nm. Within the experimental accuracy the amplitude of these three displacement vectors are the same. It thus appears that in this context the thickness of the $(CuO_2 + Ca)$ bilayer is 0.320 nm with no significant difference even with accuracy as high as 1–3 pm. Bi2212 and Bi2223 have virtually the same lattice parameters in the *a*-*b* plane resulting in no significant strain along the *c* axis. The immediate guess would then be that the intercalation of a half layer of Bi2223 in Bi2212, or vice versa, resulted in $|\mathbf{R}| = 1/2(c^{2223} - c^{2212}) = 0.310$ nm. Similarly we may expect the displacement for the intrinsic fault in Bi2212 in $R_1 = 1/2(c^{2201} - c^{2212}) = -0.325$ nm, or somewhat more because the intercalated layer of Bi2201 in Bi2212 is in lateral expansion and thus further shrinkage normal to the boundary due to the larger *a* and *b* lattice parameters in Bi2212 than in Bi2201. A possible reason for the significant discrepancy is that the reported lattice parameters are not accurate enough. In particular there are few measurements of the lattice parameters of Bi2223, an accurate set that we are aware of and use here,[16] contained a fair amount of lead. For Bi2212 and Bi2201 there is significant scatter in the lattice parameters reported in the literature. This spread is probably caused by deviations from stoichiometry. Our decade long experience from high-resolution electron microscopy in the study of Bi-based superconductors suggests that it is very difficult to synthesize the pure phases. We frequently encounter intercalations which may result in deviations from the true lattice parameter of the pure phases in diffraction experiments. Among other possibilities, a very simple explanation for this discrepancy would be that it is the lattice parameter of Bi2212 we use in this study that is about 0.02 nm too high. The difference between Bi2201 and Bi2223 are four bilayers that amounts to a thickness of $(c^{2223} - c^{2201})/4 = 0.318$ nm for each $(CuO_2 + Ca)$ bilayer. We see that there are several parameters that have to be known better to discuss our accurate measurements of displacement vectors, further. Our finding is that with reference to Bi2201, the thickness of the first bilayer added, which has a SrO layer on one side and a CuO_2 layer on the other side, is 0.320 nm. The same is the thickness of the next bilayer which can be looked upon as having a CuO_2 on one side and Ca on the other.

Lattice expansion at a pure twist boundary is generally very small and difficult to measure experimentally. The widely used coincidence-site-lattice model considering two sets of screw dislocations to accommodate the boundary misorientation does not give rise to any lattice displacement in the direction of the rotation axis, or boundary plane normal. On the other hand, such a lattice expansion has been inferred as the general trend from theoretical studies and computer modeling.[22,23] In the case of twist boundaries in Bi2212, measurements of the distance between the BiO double layers at the boundary and away from the boundary using HREM has failed to detect possible lattice expansion[7] that was considered to be negligibly small due to the soft bonding of the Bi atoms normal to the boundary. However, due to the high sensitivity to the displacement of the technique we used in the present work, we measured an expansion of 0.03 ± 0.01 nm for the three boundaries we have studied so far. Further work is needed to assess the expansion as a function of the twist angle and density of interfacial coincidence sites. The coherent convergent electron-beam diffraction technique we developed appears to be a technique of sufficient high accuracy to address this challenge even in complex system such as high-temperature superconductors. It is robust in that it is insensitive to microscope and crystal parameters and the exact orientation of the crystal relative to the direction of the incident electron beam. Our values of the expansion of 0.03 nm is within the range reported for metals and ionic materials based on atomistic modeling[23] and some HREM experiments for simpler materials.[24,25] Although the Bi-based superconductors are oxides, the region around the neighboring BiO planes is considered to be metallic, and the fact that the crystal easily cleaves in between the two BiO planes suggests weak bonding across these planes that are separated by a distance as large as 0.340 nm. Based on the bond valence concept, using the atomic positions for Bi2212 from Ref. 15, and the bond valence parameters of Brown and Altermatt [26], we find that the valence of the Bi-O bond across the two neighboring BiO planes is only 0.03, in each the four Bi-O bonds in the *a*-*b* plane is 0.2, and in the Bi-O bond pointing towards to the Sr-O plane is as high as 1.3. With this weak ionic bonding across the BiO layers and the very strong bonding in the opposite direction, one may expect that the two crystals after twisting may act as two intact crystals with negligible relaxation of the outermost atomic layers, as suggested by HREM observations and calculations.[7] The weak ionic bonding across the BiO layers suggests that there is no need for strong interactions across the twist boundary to saturate broken bonds.

Knowledge of interfacial bonding and hence the displacement is of great importance in understanding the structure-properties relationships of polycrystal materials. The displacement is directly related to the boundary interfacial energy and the surface energy of the two crystals that form the boundary. This is discussed in detail in the Appendix, together with a discussion of various mechanical and thermal properties at the boundary. There it is shown that a simple phenomenological model of interplanar interactions, expressed in terms of suitably scaled variables, can be constructed in terms of a single dimensionless material parameter Ed_0/Γ_s, where E is the elastic modulus for the relevant

TABLE I. Effective values of the power-law exponent n in Eq. (A4), chosen to match experimental data for various elements and compounds.

Element or compound	Ed_0/Γ_s	n_{eff}	Ref.
Cu (fcc)	50.7	7.4	31, 32
Fe (bcc)	15.1	5.4	31, 32
CaF_2	49.8	7.4	31, 32
NaCl	61.5	7.9	31, 32
C, graphite (interplanar)	33.1	6.5	33
C, diamond (111 direction)	32.7	6.5	34

cleavage strain, d_0 is the interplanar separation for the twist boundary planes in a perfect (untwisted) crystal, and Γ_s is the surface energy of a crystal terminated by the twist boundary plane. (Cleaving a perfect crystal at the twist boundary plane requires an energy of $2\Gamma_s$.) In the Bi2212 case, the relevant planes are those of the BiO double layer, which are known to cleave rather easily, although the bonding in Bi2212 is predominantly ionic in character. Thus we chose the single parameter of the model, the power-law exponent, to be midway between that for van der Waals bonded graphite sheets and that for ionically bonded NaCl (see Table I). With this choice, and the experimentally measured value, 0.13, of the fractional expansion of the interplanar spacing which accompanies the twist boundary, we estimate that the value of the twist boundary energy is about 85% of the value of the energy of a BiO-terminated free surface and that the elastic stiffness of the BiO double layer at a twist boundary is about 40% of its value in a perfect crystal. (see Table II for details.) This expansion and softening of the twist boundary is likely to facilitate the insertion there of interstitial oxygen ions, thus resulting in oxygen segregation and overdoping of the boundary. This could be an important factor in the absence of superconducting weak-link behavior at such boundaries.[6,7]

TABLE II. Mechanical and thermal properties of a twist boundary in the BiO double layers of Bi2212, scaled by values for a perfect crystal. These values were calculated based on the expansion of the interplanar spacing obtained using Parodi, $\varepsilon^*=0.13$, together with Eq. (A4) with the exponent $n=7$; the uncertainty in the values were calculated with $n=6$ and 8.

Quality	Scale value
Grain-boundary energy: $\Gamma_{\text{gb}}/\Gamma_s$	0.85 ± 0.15
Relaxation of grain-boundary energy due to displacement, $\Delta\Gamma_{\text{gb}}/\Gamma_s$	-0.30 ± 0.05
Elastic modulus E_{gb}/E_0	0.40 ± 0.05
Cleavage stress $\sigma_{\text{gb}}/\sigma_0$	0.50 ± 0.05
Thermal-expansion coefficient $\sigma_{\text{gb}}/\sigma_0$	2.2 ± 0.03

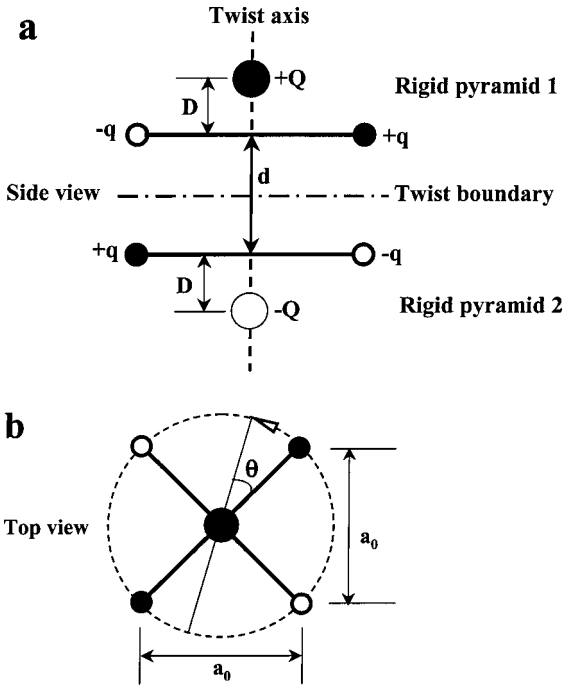

FIG. 12. A toy model which demonstrates the displacement which accompanies a twist grain boundary.

ACKNOWLEDGMENT

This work was supported by Division of Materials Sciences, Office of Basic Energy Science, U.S. Department of Energy, under Contract No. DE-AC02-98CH10886.

APPENDIX: PHENOMENOLOGICAL MODEL OF THE LATTICE DISPLACEMENT AT TWIST GRAIN BOUNDARIES AND APPLICATIONS TO Bi2212

First, we consider a simple ''toy model'' to illustrate the origin of perpendicular displacements at twist grain boundaries. This model is shown in Fig. 12 and consists of two rigid pyramidal halves which can be rotated relative to each other (twisted) about a common axis. The predominant cohesion is provided by the Coulombic interaction between the two ions with charge $(\pm Q)$ at the top of the pyramids. This mimics that Madelung potential from the crystal on either side of the boundary. The net charge of each square planar ionic array at the bottom of each pyramid (one of which is seen from above in the top view in the figure) is zero (no monopole charge) but it has a quadrupole moment. This is a proxy for the BiO planes in the Bi2212 structure. Thus the Coulombic interaction between the two planes varies from attractive to repulsive as the twist angle of the boundary between the two planes brings ions with like charges into close proximity at a 90° rotation away from the low-energy configuration with unlike charges facing each other. There is a core-overlap repulsive interaction between the ions facing each other across the plane of the twist boundary, which for simplicity we take to be independent of the twist angle. It is straightforward to calculate the resulting equilibrium spacing across the twist boundary and the relaxed grain boundary energy as the angle of twist increases, for a given choice of

the parameters Q, q, D, and a_0 (which are constants) together with a suitable description of the repulsive interaction. It is also easy to calculate the cleavage energy required to separate the two pyramidal halves to infinity, i.e., to create two new surfaces. Such calculations are trivially easy to make for this model, but rather than displaying them explicitly, since the numerical results of such a simple model are not expected to be quantitatively meaningful, we will summarize a few general conclusions which may be drawn from the behavior of the model. We will then introduce a phenomenological model based on the results which can be used to discuss the expected behavior of twist boundaries for crystals with various types of interatomic bonding, to place the experimental results for Bi2212 in context, and to estimate the likely effects of such a boundary on the local elastic modulus and thermal-expansion coefficient.

The numerical results for the toy model show that the fractional displacement at equilibrium ε^* across the boundary varies with the angle of twist θ and can be expressed as a function of $\Gamma_{gb}(\theta)/2\Gamma_s$ where Γ_{gb} is the relaxed twist boundary energy and $2\Gamma_s$ is the cleavage energy, with Γ_s the surface energy. Call this ratio of energy R, and let R_0 denote the same ratio if no displacement across the twist boundary is permitted. If the parameter R is greater than unity, the crystal (in this case, the bipyramid) will spontaneously cleave, i.e., the crystal is unstable. The fractional equilibrium displacement ε^* diverges as R approaches unity. The numerical results can be described approximately by

$$\varepsilon^* \approx \frac{kR}{(1-R)^{\alpha}}, \tag{A1}$$

where k and α are numerical constants, the values of which depend on the parameters of the model as will be described in the context of the phenomenological model to be discussed below.

Consider the form of the cleavage energy of the bipyramid toy model in the ''narrow fiber'' limit of the parameters, i.e., the cleavage plane spacing d is large compared with scale of interatomic spacings a_0 and D, $d \gg a_0$, D. In this case the interplanar cohesive energy V as a function of cleavage plane spacing is given by a monopole-monopole attraction cohesive force, an interplanar overlap repulsion, and a quadrupole-quadrupole interaction which depends on the twist boundary misorientation θ:

$$V = -\frac{Q^2}{d} - \frac{3q^2a_0^4}{d^5}\cos 2\theta + \frac{K}{d^n} + 2\Gamma_s, \tag{A2}$$

where the repulsive force exponent n is typically in the range from 5 to 12.[27] The zero of energy is chosen to be that for no twist boundary ($\theta = 0$) and for the equilibrium spacing d_0 where $d\varepsilon/dd = 0$. This form suggests a simple phenomenological model for the cleavage energy of an infinite crystal with a twist boundary for more general type of bonding.

Let V be the energy per unit area as a function of the interplanar separation d:

$$V(d,\theta) = \frac{K_n}{d^n} + \frac{K_m \cdot f(\theta)}{d^{n-m}} - \frac{K_p}{d^{n-p}} + 2\Gamma_s, \tag{A3}$$

where the first term is the interplanar overlap repulsion, the second term is a multipolar interplanar interaction which gives rise to the twist boundary energy for misorientation angle θ, the third term is the interplanar cohesion which resists cleavage, and the final term is the cleavage energy. The phenomenological coefficients K_n, etc., are to be determined from the equilibrium interatomic spacing, elastic moduli, etc. This power-law form for the cleavage energy is similar to those widely used to describe the mechanical and thermal properties of solids under conditions of finite strain,[28] but with the addition of the second term which describes the energy of the twist boundary.

In order to discuss the twist boundary energy and its resulting displacement, we will further simplify the model by putting it into a scaled form and picking a plausible particular relation between the power-law exponents of the various terms. We choose the exponents n and p to be 2 and 4, respectively, which yields a one-parameter model for which the equilibrium displacement can be found from a simple quadratic equation. For example, when the repulsive term exponent is chosen to be 7, the twist boundary exponent is 5 (as in quadruple-quadruple interaction) and the cohesive exponent is 3. The value of the latter exponent is unlikely to be 1, as in the toy model, because cleavage planes and twist boundary planes are not likely to interact by simple unscreened Coulomb interactions. For example, in a simple metal the long-range cohesive term can be approximated by Lifshitz polarization interactions[29] which yields a cohesive exponent of 2, corresponding to an exponent $n=6$, whereas for the graphene sheets in graphitic structures,[30] van der Waals interactions yield an interplanar cohesive exponent of 4, which leads to an exponent $n=8$ in our model. In scaled form the interplanar energy is given by

$$\nu = \frac{n-4}{4}\cdot\frac{1}{\eta^n} + \frac{R_0(\theta)}{\eta^{n-2}} - \frac{n}{4}\cdot\frac{1}{\eta^{n-4}} + 1. \tag{A4}$$

where ν is the interplanar cohesive energy per unit area scaled by the cleavage energy $2\Gamma_s$, η is the interplanar spacing d scaled by the equilibrium value with no twist boundary present (i.e., a perfect crystal); η can be expressed in terms of a cleavage strain, i.e., as $1+\varepsilon$. R_0 is the scaled twist boundary energy, $\Gamma_{gb}(\theta)/2\Gamma_s$, when no displacement across the boundary is permitted. After allowing displacement, R_0 decreases to its relaxed value R with an accompanying displacement, expressed as a strain $\varepsilon^* = \Delta d/d_0$. The latter is measured using the Parodi method. If we choose a value of the power-law exponent n, then we can use the observed value of ε^* to calculate the ratio of the relaxed twist boundary energy to the cleavage energy, $\Gamma_{gb}(\theta)/2\Gamma_s$. This is done using Eq. (A1), which describes quite accurately both the numerical results from the toy model as well as those from the phenomenological model, Eq. (A4). (The numerical values of parameters k and α depend on the particular model, and for the phenomenological model they depend in particular on the choice of the power-law exponent n.) In addition, for a given choice of n one can easily calculate the values of several mechanical and thermal properties at the twist

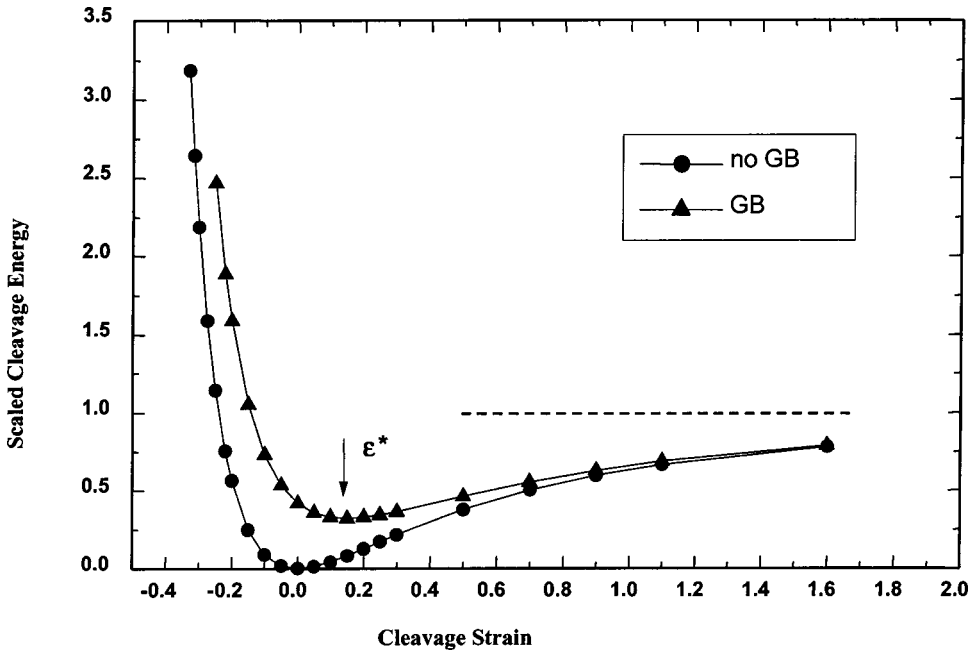

FIG. 13. Scaled interplanar interaction (cleavage energy) as a function of cleavage strain, calculated from Eq. (A4) with cohesive exponent $n=6$ and the uncleaved twist boundary energy R_0 chosen to yield a twist boundary displacement ε^* of 0.13.

boundary scaled by those for the perfect crystal, as discussed below (see Fig. 13).

A dimensionless ratio of physical properties, Ed_0/Γ_s, where E is the elastic modulus associated with uniaxial cleavage strain, serves as a basis to make a choice for n, based on values for various solids with different types of bonding and structures. It is easily shown from Eq. (A4) for the perfect crystal case $(R_0=0)$ that

$$\frac{Ed_0}{\Gamma_s}=2n(n-4). \tag{A5}$$

Thus one can use experimental data for various substances to find an effective value of n, which matches the experimental data, as listed in Table I. Note that since Eq. (A4) utilizes scaled values of parameters, the power-law exponent n is a measure only of the shape of the interplanar potential. This is also true of the dimensionless parameter Ed_0/Γ_s, as illustrated by Eq. (A5). The data in Table I reflect this. Note that the ionic crystals CaF_2 and NaCl have almost the same value, while van der Waals bonded graphite planes and covalently bonded close-packed planes of diamond have the same value, perhaps coincidentally. The data of Table I indicate that it is likely that the value of n appropriate to the BiO double layer lies in the range between 6 and 8. An intuitive guess, based on the easy cleavage of the BiO double layer and the fact of the predominantly ionic bonding of Bi2212, suggests an n value somewhere between that of graphite and NaCl. Thus we choose a value $n=7$ to calculate various scaled mechanical and thermal properties for the BiO double layer twist boundary in Bi/2212, and use values for $n=6$ and 8 to estimate the uncertainty in the calculation. The results are collected in Table II. These results suggest that the twist boundary energy is about 85% of the energy of a BiO-terminated surface and that the cleavage strength at a twist boundary is about 50% lower than that for a perfect crystal. The twist boundary region is softer than the perfect BiO double layer; the elastic modulus is reduced by 60%. The expansion and softening should make it easier to accommodate oxygen interstitial atoms at a twist boundary than it is in the BiO double layers in perfect regions of the crystal, thus resulting in oxygen segregation and a consequent overdoping of twist boundaries. This could be an important factor in explaning the experimental observations of strongly coupled grain boundaries in bicrystal Bi2212 experiments on superconducting critical current.[6,7]

*Corresponding author. Email address: zhu@bnl.gov

[1] Z. Cai and Y. Zhu, *Microstructures and Structural Defects in High-Temperature Superconductors* (World Scientific, Singapore, 1998); Y. Zhu, J. M. Zuo, A. R. Moodenbaugh, and M. Suenaga, Philos. Mag. A **70**, 969 (1994).

[2] J. Mannhart and P. Chaudhari, Phys. Today **54** (11), 48 (2001).

[3] D. Dimos, P. Chaudhari, and J. Mannhart, Phys. Rev. Lett. **61**, 219 (1988), Phys. Rev. B **41**, 4038 (1990).

[4] S. E. Babcock, X. Y. Cai, D. L. Kaiser, and D. C. Larbaleslier, Nature (London) **347**, 167 (1990).

[5] G. Hammert, A. Schmehl, R. R. Schulz, B. Goetz, H. Blelefeldt, C. W. Schnelder, H. Hilgenkamp, and J. Mannhart, Nature (London) **407**, 162 (2000).

[6] Q. Li, Y. N. Tsay, M. Suenaga, R. A. Klemm, G. D. Gu, and N. Koshizuka, Phys. Rev. Lett. **83**, 4160 (1999).

[7] Y. Zhu, Q. Li, N. Tsay, M. Suenaga, G. D. Gu, and N. Koshizuka, Phys. Rev. B **57**, 8601 (1998).

[8] D. R. Rasmussen, S. McKernan, and C. B. Carter, Phys. Rev. Lett. **66**, 2629 (1991).

[9] J. M. Cowley, in *Electron Diffraction Techniques*, edited by J. M. Cowley (Oxford University Press, New York, 1992), Vol. 1, p. 441.

[10] P. D. Nellist and J. M. Rodenburg, Acta Crystallogr., Sect. A: Found. Crystallogr. **A54**, 49 (1998).

[11] L. Wu, Y. Zhu, and J. Tafto, Phys. Rev. Lett. **85**, 5126 (2000).

[12] H. W. Zandbergen, W. A. Groen, F. C. Mijihoff, G. van Tendeloo, and S. Amelincx, Physica C **156**, 325 (1988).
[13] O. Eibl, Physica C **168**, 215 (1990).
[14] C. C. Torardi, M. A. Subramanian, J. C. Calabrese, J. Gopaakeishnan, E. M. McCarron, K. J. Morrissey, T. R. Askew, R. B. Flippen, U. Chowdhry, and A. W. Sleight, Phys. Rev. B **38**, 225 (1988).
[15] Y. Gao, P. Lee, P. Coppens, M. A. Subramanian, and A. W. Sleight, Science **241**, 954 (1988); Y. Gao, P. Coppens, D. E. Cox, and A. R. Moodenbaugh, Acta Crystallogr., Sect. A: Found. Crystallogr. **A49**, 141 (1993).
[16] G. Miehe, T. Vogt, H. Fuess, and M. Wilhelm, Physica C **171**, 339 (1990).
[17] K. Shibutani, T. Egi, S. Hayashi, Y. Fukumoto, I. Shigaki, Y. Masuda, R. Ogawa, and Y. Kqwate, IEEE Trans. Appl. Supercond. **3**, 935 (1993).
[18] J. Tafto, Y. Zhu, and L. Wu, Acta Crystallogr., Sect. A: Found. Crystallogr. **A54**, 532 (1998).
[19] L. Wu, Y. Zhu, and J. Tafto, Phys. Rev. B **59**, 6035 (1999).
[20] Y. Zhu, L. Wu, and J. Tafto, J. Electron Microsc. **50**, 465 (2001).
[21] M. Schofield, Y. Zhu, and L. Wu (unpublished).
[22] A. P. Sutton and R. W. Balluffi, *Interfaces in Crystalline Materials* (Clarendon, Oxford, 1995), Chap. 4.
[23] K. L. Merkle and D. Wolf, Mater. Res. Bull. **25**, 42 (1990).
[24] K. L. Merkle and D. J. Smith, Phys. Rev. Lett. **59**, 2887 (1987).
[25] K. Nadarzinski and F. Ernst, Mater. Sci. Forum **207–209**, 309 (1996).
[26] Brown and Altermatt, Acta Crystallogr., Sect. B: Struct. Sci. **B41**, 244 (1985).
[27] G. G. Hall, *Molecular Solid State Physics* (Springer-Verlag, Berlin, 1991).
[28] F. D. Stacey, Phys. Earth Planet. Inter. **128**, 179 (2001).
[29] C. W. Lung and N. H. March, *Mechanical Properties of Metals* (World Scientific, Singapore, 1999).
[30] L. A. Girifalco, M. Hodak, and R. S. Lee, Phys. Rev. B **62**, 13 104 (2000).
[31] Elastic and crystallographic data from *Handbook of Chemistry and Physics of Solids*, edited by D. R. Lide, 82nd ed. (CRC Press, Boca Raton, FL, 2001).
[32] Surface energies from J. M. Howe, *Interfaces in Materials* (John Wiley, New York, 1997). Table 3.1.
[33] L. A. Girifalco, M. Hodak, and R. S. Lee, Phys. Rev. B **62**, 13 104 (2000).
[34] J. J. Gilman, in *The Physics and Chemistry of Ceramics*, edited by C. Klingsberg (Gordon and Breach, New York, 1963), p. 240ff.